Ionizing radiation-induced acoustics for radiotherapy and diagnostic radiology applications

Susannah Hickling[a)]
Department of Physics & Medical Physics Unit, McGill University, 1001 boul Decarie, Montreal, QC H4A 3J1, Canada

Liangzhong Xiang
School of Electrical and Computer Engineering, University of Oklahoma, Norman, OK 73019, USA

Kevin C. Jones
Department of Radiation Oncology, Rush University Medical Center, Chicago, IL 60612, USA

Katia Parodi and Walter Assmann
Department of Medical Physics, Ludwig-Maximilians-Universität, Garching b. München 85748, Germany

Stephen Avery
Department of Radiation Oncology, University of Pennsylvania, Philadelphia PA19104, USA

Maritza Hobson
Medical Physics Unit, McGill University Health Centre, Montreal, QC H4A 3J1, Canada
Department of Oncology, Department of Physics & Medical Physics Unit, McGill University, Montreal, QC H4A 3J1, Canada

Issam El Naqa
Department of Radiation Oncology, University of Michigan, Ann Arbor, MI 48103-4943, USA

(Received 24 November 2017; revised 20 February 2018; accepted for publication 9 April 2017; published 18 May 2018)

Acoustic waves are induced via the thermoacoustic effect in objects exposed to a pulsed beam of ionizing radiation. This phenomenon has interesting potential applications in both radiotherapy dosimetry and treatment guidance as well as low-dose radiological imaging. After initial work in the field in the 1980s and early 1990s, little research was done until 2013 when interest was rejuvenated, spurred on by technological advances in ultrasound transducers and the increasing complexity of radiotherapy delivery systems. Since then, many studies have been conducted and published applying ionizing radiation-induced acoustic principles into three primary research areas: Linear accelerator photon beam dosimetry, proton therapy range verification, and radiological imaging. This review article introduces the theoretical background behind ionizing radiation-induced acoustic waves, summarizes recent advances in the field, and provides an outlook on how the detection of ionizing radiation-induced acoustic waves can be used for relative and *in vivo* dosimetry in photon therapy, localization of the Bragg peak in proton therapy, and as a low-dose medical imaging modality. Future prospects and challenges for the clinical implementation of these techniques are discussed. [https://doi.org/10.1002/mp.12929]

Key words: low-dose imaging, photon beam dosimetry, proton range verification, radiation acoustics, thermoacoustic effect

1. INTRODUCTION

Alexander Graham Bell discovered the thermoacoustic effect in 1880 while working on his invention of the photophone, a device to transmit sound via a beam of light, when he observed that acoustic waves were generated when a solid sample was exposed to a rapidly interrupted beam of sunlight.[1] This phenomenon whereby acoustic waves are induced following a pulse of electromagnetic radiation is commonly referred to as the photoacoustic effect; however, this implies that only photon beams are capable of generating acoustic waves. Since the induction of acoustic waves is observed after irradiation by a pulsed beam of charged or uncharged particles, the term thermoacoustic effect is more general and will be used throughout this article.

Briefly, the thermoacoustic effect can be summarized as follows. When a pulsed beam of electromagnetic radiation strikes a material the localized temperature increase leads to thermoelastic expansion and the buildup of a differential pressure distribution, which is dependent on the properties of the material as well as the radiation beam. This causes the propagation of acoustic pressure waves that can be detected using devices such as ultrasound transducers and hydrophones, which typically use piezoelectric crystals to generate an electrical signal in response to mechanical stress/pressure. Information regarding the pressure distribution induced following a pulse of radiation can be extracted from the detected time-varying pressure signals, and an image of the initial differential pressure distribution can be reconstructed using signals acquired at multiple angles surrounding the irradiated region.

The thermoacoustic effect has been widely studied and applied to medicine as early as the 1980s when it was

proposed that it could be exploited to image tissue.[2] This idea gave rise to photoacoustic imaging, which uses optical photons from a laser source to induce acoustic waves. Contrast in photoacoustic imaging arises from the differential absorption of optical photons in the body, thus structures such as hemoglobin, lipids, and melanin can be imaged.[3] Photoacoustic imaging has been widely used as a preclinical imaging technique and has recently been translated to the clinic, primarily for superficial applications such as breast cancer imaging.[4] Similarly, the term thermoacoustic imaging refers to an imaging modality that uses a pulsed microwave source to image tissues based on their dielectric properties. While it has been applied to cancer imaging, microwave thermoacoustic imaging is less widespread than photoacoustic imaging.[5] Although both imaging modalities are rapidly advancing, photoacoustic techniques are limited by the penetration depth of optical photons, while microwave thermoacoustic imaging is often hindered by poor dielectric contrast.

The goal of this article is to explore how the detection of the acoustic waves induced by ionizing radiation beams can be applied in radiation therapy and diagnostic radiology. As early as 1981, it was proposed that detecting the acoustic waves generated by therapeutic radiation beams could serve as a means for verifying treatment delivery.[2] While promising work was done in this area in the 1980s and early 1990s, few studies were published between that time and 2013, when interest in the field was renewed. Since 2013, ionizing radiation-induced acoustics has been applied to three main areas: (a) linear accelerator (linac) photon beam dosimetry; (b) proton therapy range verification; and (c) medical imaging. Many studies have been published in recent years demonstrating the feasibility and potential of using ionizing radiation-induced acoustics in these three areas. It is now time to work on translating these promising initial studies into clinically viable techniques. All three applications of ionizing radiation-induced acoustics share the same physics principles, thus advancements in one application are highly relevant to the others.

This article provides a future outlook of the field of radiation-induced acoustics for radiotherapy and diagnostic radiology applications and is divided into three focus areas:

1. Linac photon beam dosimetry
2. Proton therapy range verification
3. Medical imaging.

The article begins with an initial background review of the theory behind ionizing radiation-induced acoustics and initial studies in the field that have motivated recent work in the above three areas.

2. THEORY

The thermoacoustic effect states that acoustic waves are induced in an object following a pulse of radiation. The sections below detail how a beam of ionizing radiation deposits dose and heat energy within an object, and how this leads to a temperature rise, thermoelastic expansion, and ultimately the generation and propagation of acoustic waves throughout the irradiated object. The ability to reconstruct images based on the detection of these acoustic waves is also discussed.

2.A. Deposition of dose by ionizing radiation

The primary quantity of interest in radiation therapy is radiation dose, which is defined as the amount of energy deposited per unit mass by a beam of ionizing radiation and quantified using the unit Gray (1 Gy = 1 J/kg). Beams of charged particles, such as protons or electrons, are considered directly ionizing radiation since they deposit their energy through Coulombic interactions within the media they traverse. Beams of uncharged particles, such as photons, are classified as indirectly ionizing radiation since they must undergo interactions to release secondary charged particles which then deposit their energy through Coulombic interactions.

Due to the stochastic nature of energy deposition, Monte Carlo (MC) techniques are considered to be the most accurate way of calculating radiation dose.[6] MC techniques simulate particle trajectories using random numbers to sample the probability density functions of potential interactions a particle may undergo as it traverses a medium. A number of MC codes are used for radiation therapy dose calculation applications, including EGSnrc,[7] Geant4,[8] MCNP,[9] Fluka,[10] and PENELOPE.[11] MC techniques are commonly used in ionizing radiation-induced acoustics simulations to obtain the dose distribution following a pulse of radiation.

2.B. Heat energy and temperature increase

Nearly all of the energy deposited by a beam of ionizing radiation is converted to heat energy. The heat defect, which is dependent on the type of ionizing radiation and material being irradiated, refers to the amount of energy not deposited as heat energy, and therefore does not contribute to a temperature increase. Chemical reactions are the primary contributor to the heat defect, with exothermic reactions leading to a heat defect less than zero and endothermic reactions resulting in a positive heat defect. A small amount of energy also goes into radiation-induced acoustic and optical emissions.[12] The heat defect, k_{HD}, is related to deposited ionizing radiation dose, D, through:

$$D = \frac{E}{m} = \frac{E_H}{(1 - k_{HD})m}, \tag{1}$$

where E is the total energy deposited in a volume of mass m and E_H is the deposited heat energy.

Assuming that the heat energy is deposited in a shorter time than it takes the density or volume of the irradiated medium to change, the deposition of heat energy results in a temperature rise, ΔT, given by:

$$\Delta T = \frac{H}{\rho_0 \cdot C_v}, \tag{2}$$

where H is the heat energy density, ρ_0 is the mass density and C_v is the constant volume specific heat capacity.

2.C. Derivation of initial temperature–pressure initial conditions

To understand how a temperature increase results in the generation of pressure waves, it is necessary to consider the following two thermodynamic identities[13]:

$$\Delta\rho = \rho_0 K_T \Delta p - \rho_0 \beta \Delta T \tag{3}$$

and

$$v_s^2 = \frac{C_p}{K_T \rho_0 C_v}, \tag{4}$$

where K_T is the isothermal compressibility coefficient, p is the differential pressure, β is the isobaric expansion coefficient, v_s is the speed of sound, and C_p is the specific heat capacity at constant pressure.

Again, it is assumed that heat energy is deposited on a time scale shorter than it takes for the medium density to change, thus $\Delta\rho$ in Eq. (3) is set to zero and the identity is rearranged to yield:

$$\Delta p = \frac{\beta}{K_T} \cdot \Delta T. \tag{5}$$

Inserting Eq. (2) into Eq. (5) yields:

$$\Delta p = \frac{\beta}{K_T \rho_0 C_v} H \tag{6}$$

and combining with Eq. (4) results in:

$$\Delta p = \frac{\beta v_s^2}{C_p} H, \tag{7}$$

which relates the pressure increase to the deposited heat energy through material specific constants. The isobaric expansion coefficient, speed of sound, and specific heat capacity at constant pressure are all properties of the material being irradiated, and combine to form the Grüneisen coefficient, Γ, a dimensionless, material specific constant that indicates the conversion efficiency between the deposited heat energy and pressure variation:

$$\Gamma = \frac{\beta v_s^2}{C_p}. \tag{8}$$

Thus, the initial pressure distribution induced following a pulse of ionizing radiation at a given location, $\mathbf{r}$, can be related to deposited heat energy through:

$$p_0(\mathbf{r}) = \Gamma(\mathbf{r}) \cdot H(\mathbf{r}). \tag{9}$$

Finally, this initial condition can be rewritten in terms of ionizing radiation dose deposited at a given location, $D(\mathbf{r})$, as:

$$p_0(\mathbf{r}) = \Gamma(\mathbf{r}) \cdot D(\mathbf{r}) \cdot \rho(\mathbf{r}) \cdot (1 - k_{HD}(\mathbf{r})). \tag{10}$$

2.D. Propagation of acoustic pressure waves

The spatially varying differential pressure distribution induced following a pulse of radiation causes the generation of acoustic waves, which propagate provided that the irradiated material is elastic and inertial. This is governed by the thermoacoustic wave equation, which describes the evolution and the propagation of the acoustic pressure waves following a pulse of deposited heat energy:

$$\nabla^2 p(\mathbf{r}, t) - \frac{1}{v_s^2} \frac{\partial^2}{\partial t^2} p(\mathbf{r}, t) = -\frac{\beta}{C_p} \frac{\partial}{\partial t} H(\mathbf{r}, t). \tag{11}$$

The thermoacoustic wave equation can be solved numerically with a Green's function approach to yield the pressure at a given time, t, and location, $\mathbf{r}$, assuming an impulsive heating source[14]:

$$p_\delta(\mathbf{r}, t) = \frac{1}{4\pi v_s^2} \frac{\partial}{\partial t} \left[\int d\mathbf{r}' \frac{p_0(\mathbf{r}')}{|\mathbf{r} - \mathbf{r}'|} \delta\left(t - \frac{|\mathbf{r} - \mathbf{r}'|}{v_s} \right) \right]. \tag{12}$$

Thus far, it has been assumed that heat energy is deposited instantaneously. For this assumption to hold, the heating pulse must satisfy both thermal and stress confinement conditions, meaning the pulse of ionizing radiation must be shorter than the thermal relaxation time, τ_{th}, and the stress relaxation time,τ_s:

$$\tau_{th} = \frac{d^2}{\alpha_{th}} \tag{13}$$

$$\tau_s = \frac{d}{v_s} \tag{14}$$

where d is the desired spatial resolution and α_{th} is the thermal diffusivity of the material.[14] Considering a desired spatial resolution of 1 mm in water, Eq. (13) indicates that for a thermal diffusivity of water at room temperature of 0.143 mm^2/s the thermal relaxation time is 7 s. As per Eq. (14), assuming a speed of sound in water of 1480 m/s yields a stress relaxation time of 0.68 μs. While the thermal confinement condition is easily satisfied in ionizing radiation-induced acoustics applications, pulse lengths are typically longer than the stress relaxation time. In order to account for the lack of stress confinement, the solution given by Eq. (12) must be convolved with the temporal profile of the heating pulse, *S(t)* [14]:

$$p(\mathbf{r}, t) = \int_{-\infty}^{+\infty} dt' p_\delta(\mathbf{r}, t - t') S(t'). \tag{15}$$

S(t) is dependent on the source of ionizing radiation. In the case of photon beams produced by clinical linear accelerators *S(t)* is often rectangular in shape,[15] while clinical synchrocyclotrons produce proton beams with Gaussian shaped pulses,[16] both with full-width half-maximum lengths on the order of several microseconds.

Before moving on, it is worth briefly discussing Eq. (12) in more depth. As is shown in the delta-function term in Eq. (12), time and distance are linked. The pressure wave that reaches point $\mathbf{r}$ at time t originates at a distance $|\mathbf{r}-\mathbf{r}'| = t \cdot v_s$. This distance specifies a sphere centered at the detection point that gets bigger as time increases. The magnitude of pressure waves that reach the detector are related to the initial pressure distribution that intersects with this sphere. Mathematically, due to the delta-function term, the integral reduces to a spherical surface integration of the initial pressure distribution with an inverse distance amplitude scaling, hence the $1/|\mathbf{r}-\mathbf{r}'|$ term. The time derivative can be interpreted in two ways. The pressure waves are shaped by the radial gradient of the spherical surface integration of the initial pressure distribution since the time derivative can be conceptually translated into a spatial derivative due to the time/distance relationship. Due to the properties of convolution, when Eq. (15) is considered the time derivative can instead be applied directly to the temporal profile of the heating pulse, *S(t)*. Thus, the detected pressure waves will be related to the time derivative of the heating pulse. Hence, acoustic emissions are only induced by temporally varying radiation sources.

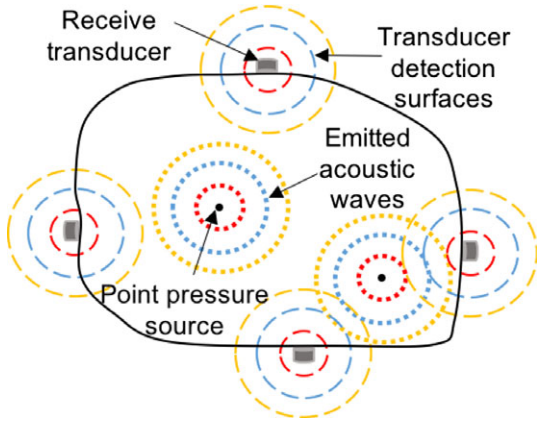

FIG. 1. Schematic demonstrating the propagation and detection of induced acoustic waves. The black dots represent point pressure sources, and the dotted lines represent the resulting pressure waves. Different colors represent the position of the induced acoustic wave at subsequent times following irradiation. More complicated pressure distributions can be treated as the superposition of many point sources. The dashed circles surrounding each transducer represent the transducer detection surfaces, with each color corresponding to a different detection time equal to the distance from the transducer divided by the speed of sound in the medium.

2.E. Image reconstruction

The goal of image reconstruction in ionizing radiation-induced acoustics is to reconstruct an image of the initial pressure distribution induced following the pulse of radiation, as given by Eqs. (9) and (10). To reconstruct such an image, pressure signals need to be acquired tomographically, i.e., at multiple angles surrounding the irradiated object. The most basic way of reconstructing the initial pressure distribution is by back-projecting the detected time varying pressure signals, $p(\mathbf{r}, t)$, using the universal back-projection algorithm[17]:

$$p_0(\mathbf{r}') = \int_S d\Omega_0 p(\mathbf{r}, t)\Big|_{v_s t = |\mathbf{r}-\mathbf{r}'|}, \tag{16}$$

where Ω_0 refers to the solid angle of the entire detection surface S considering a source point at $\mathbf{r}'$. The universal back-projection algorithm has been proven to be exact for spherical, cylindrical, and planar detection geometries, however, it is unable to account for irregular geometries or material heterogeneities.[18] It is important to emphasize that unlike traditional computed tomography (CT) back-projection, pressure signals are back-projected on a spherical surface, rather than along a line as in CT, due to the spherical nature of pressure wave propagation. Fig. 1 demonstrates this principle.

Another commonly used algorithm for thermoacoustic reconstruction problems is time reversal, which considers the detected time-varying pressure signals as a pressure source. The algorithm transmits the detected signals back into the medium in time reversed order using numerical methods, such as time domain finite difference[19] and k-space pseudospectral[20,21] techniques. Time reversal algorithms are valid for any closed geometry and can account for material heterogeneities and signal attenuation.[22] As a result, they are more accurate but more computationally intensive than back-projection based methods.

3. INITIAL IONIZING RADIATION-INDUCED ACOUSTICS STUDIES

3.A. Early studies

The first reported study to demonstrate the emission of acoustic waves by ionizing radiation was in the particle physics context, where the acoustic waves induced by a 200 MeV proton beam produced by a linear accelerator and a 158 MeV cyclotron beam were detected using a hydrophone in a water tank.[23] This study comprehensively investigated how the detected acoustic signal depended on the proton beam diameter, the amount of energy deposited, the distance between the proton beam and the hydrophone, and the irradiated medium. Results were consistent with the thermoacoustic effect, thus other possible mechanisms for the formation of acoustic waves, such as microbubble implosion and molecular dissociation, were ruled out.

The experimental observation of acoustic waves induced by an x-ray beam was first reported in 1983.[24] Various metals were irradiated by a synchrotron x-ray beam, and the induced acoustic waves were detected by an ultrasound transducer. The thermoacoustic effect was first applied to x-ray dosimetry in 1983 when a cell containing a microphone was constructed to absorb a kV x-ray beam.[25] A linear relationship between the x-ray beam intensity and the induced acoustic signal was observed, and the authors recognized the possibility of expanding this technique to dosimetry measurements of other radiation beams.

Following these initial developments, it was shown that the acoustic waves induced by clinical therapeutic electron,[26] photon,[27] and proton[28] beams were detectable in water, indicating that acoustic dosimetry techniques could be feasible in a radiotherapy setting. A breakthrough in the field occurred in 1995 when Hayakawa et al. demonstrated the detection of acoustic waves *in vivo* during proton therapy treatment of a hepatic patient.[29] Fig. 2 shows the detected hydrophone signal overlaid on the patient CT scan and treatment plan. Peaks in the acoustic signal were shown to correspond to dose distribution gradients and anatomical boundaries. The authors further speculated on the possibility of using a transducer array surrounding the patient to image the three-dimensional (3D) dose distribution, as well as combining this technique with diagnostic ultrasound to register dosimetric information onto an anatomical image.

3.B. Revitalization of the field

Despite the promising results in these early studies, very little work was done regarding the use of ionizing radiation-induced acoustics in medicine until recently. In early 2013, Xiang et al. proposed x-ray acoustic computed tomography (XACT), an imaging modality that uses a pulsed x-ray beam to induce acoustic waves.[30] They experimentally demonstrated the ability to image a lead rod embedded in chicken breast tissue with a clinical linac photon beam by rotating a transducer around the sample and detecting the induced pressure waves at 200 positions surrounding the object. Later that year, Stantz et al. presented an abstract demonstrating, through computer simulations, the feasibility of using radiation induced-acoustic principles to map three-dimensional proton distributions as a method of localizing the Bragg peak.[31] These studies, along with recent advancements in photoacoustic imaging technologies and the need for volumetric x-ray dosimetry measurements and accurate range verification in proton therapy, triggered numerous publications in this field over the past 5 yr. The following sections detail recent studies and provide a future outlook on the potential applications and current challenges of ionizing radiation-induced acoustics in three main areas: linac photon beam dosimetry, proton therapy range verification, and medical imaging.

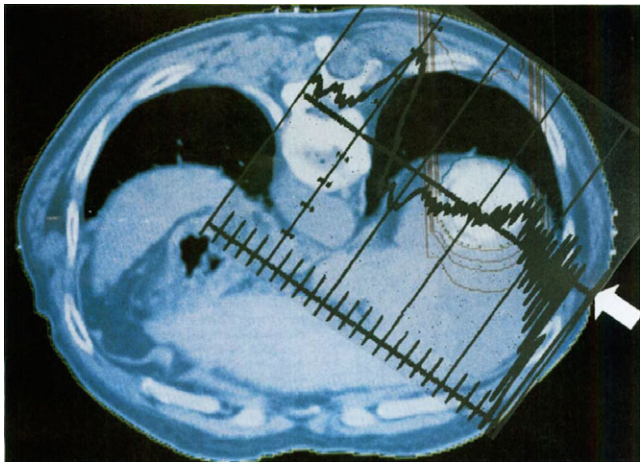

FIG. 2. CT scan and treatment plan of a hepatic patient undergoing proton radiotherapy. The arrow represents the position of the hydrophone, and the detected acoustic signal is superimposed onto the CT scan. The isodose curves correspond to the planned dose distribution. Reprinted with permission from Ref. [29].

4. LINAC PHOTON BEAM DOSIMETRY

4.A. Motivation

Dosimetry is a crucial part of photon beam radiotherapy to ensure that the delivery of radiation to the patient is well characterized and accurately known. Reference or relative dosimetry measurements in a phantom are used for beam characterization, treatment planning and quality assurance, while *in vivo* dosimetry measurements are made during treatment to directly measure the dose received by the patient. Due to the increasing complexity of linac treatment delivery techniques, such as intensity modulated radiation therapy (IMRT) and volumetric modulated arc therapy (VMAT), there is an increased need for volumetric dosimetry techniques to accurately measure the dose delivered to a phantom and to verify that treatment delivery matches the planning objectives.[6] Additionally, the International Atomic Energy Agency (IAEA) suggests that *in vivo* dosimetry should be used for patients that are receiving treatment via novel delivery techniques, after software or equipment changes, in hypofractionated treatments, and curative treatments where the dose received is potentially close to surrounding normal tissue tolerance.[32] These advancements and recommendations have necessitated the development of novel efficient and volumetric dosimetry techniques.

By detecting the acoustic waves induced in an object following irradiation by a linac x-ray beam, XACT forms images that can be related to radiation dose. As such, it has long been proposed that XACT could be used for a variety of dosimetry applications. After the recent initial demonstration of XACT,[30] various groups have worked on applying XACT to radiotherapy dosimetry applications in two main areas: relative water tank dosimetry and *in vivo* dosimetry.

4.B. Recent work

Initial studies applying XACT to linac photon beam dosimetry focused on the detection of the acoustic waves induced following the irradiation of metal blocks due to the high Grüneisen coefficient of metals and, consequently, the resulting large induced acoustic signal-to-noise ratio (SNR). The detection of such induced acoustic waves was demonstrated using a single element immersion transducer,[15,33] a hydrophone,[34] and a commercial diagnostic ultrasound transducer.[35] Additionally, the effect of changing different set-up parameters and the link between deposited dose and acoustic signal were systematically investigated and analyzed.[15] During this time, a comprehensive computer simulation

workflow combining Monte Carlo dose calculations and acoustic wave transport techniques was developed to guide experimental investigations in this area. This simulation tool was validated experimentally using simple geometries with metal block measurements.[15]

Later studies investigated using XACT to image dose distributions of various shapes and sizes in a homogeneous water tank.[36] Experimental XACT images were obtained by keeping an immersion ultrasound transducer stationary while the linac collimator was rotated. Transducer signals were acquired every 6° around the radiation field and images were reconstructed using a simple back-projection algorithm. Profiles extracted from XACT images were compared to ion chamber measurements to verify the linear relationship between XACT image intensity and delivered radiation dose. Fig. 3 demonstrates the ability of XACT to image a puzzle piece shaped field and the agreement between profiles extracted from experimental and simulated XACT images and ion chamber measurements. Of note is the negative intensity ring artifact surrounding the radiation field present in both simulated and experimental images, likely due to the limited transducer bandwidth. A subsequent XACT characterization study demonstrated that XACT images of acceptable SNR can be formed at a dose level as low as 11.6 mGy, and that changes in field size of 4 mm, field location of 2 mm, and field magnitude of 3% are detectable with the above implementation of XACT.[37] These latest studies demonstrated the viability of using XACT as a relative water tank dosimetry technique in a clinical radiotherapy environment.

The possibility of using XACT for *in vivo* dosimetry has been investigated through simulations.[38,39] In such simulations, the initial pressure distribution following a pulse of irradiation was calculated using Monte Carlo dose simulations[7] and Eq. (10). The MATLAB toolbox k-Wave[21] was then used to model the propagation of the resulting acoustic waves and obtain the time-varying pressure signal at the simulated transducer location. The first study in this area investigated using a circular array of transducers enclosing the pelvic region to reconstruct the dose deposited during a prostate treatment.[38] It was concluded based on the amplitude and the frequency of the simulated pressure waves that the induced acoustic signal should be experimentally detectable *in vivo*; however, the need to have an ultrasound transducer array surrounding the patient during treatment could be practically challenging. This led to a study investigating the use of a single transperineal ultrasound transducer to detect the acoustic waves induced during a prostate VMAT treatment.[39] The simulated transducer signal was backprojected onto the patient CT and peaks in the acoustic signal were shown to correspond to gradients in the dose distribution. This principle is demonstrated in Fig. 4, where the detection geometry is shown in Fig. 4(a) and the dose profile and back-projected acoustic signal along the projection line are displayed in Fig. 4(b). Additionally, the ability to detect set-up errors of 3 mm based on the temporal shift of the signal was demonstrated.

4.C. Future outlook

XACT is a promising technique for water tank dosimetry, and with further developments could be used for routine relative dosimetry measurements such as percent depth dose curves, dose profiles, tissue phantom ratios, and 2D/3D

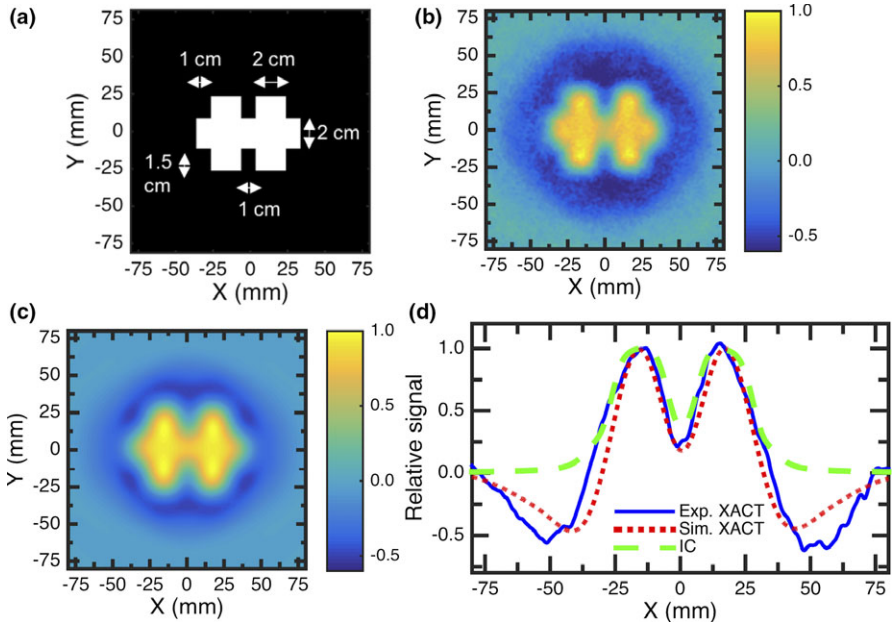

FIG. 3. (a) Block diagram of a puzzle piece shaped radiation field, where white regions represent the primary radiation beam. (b) Experimental and (c) simulated XACT images of the field. (d) Comparison of profiles extracted from experimental and simulated XACT images to ion chamber measurements along the X-axis at $Y = -15$ mm. Reproduced with permission from Ref. [36].

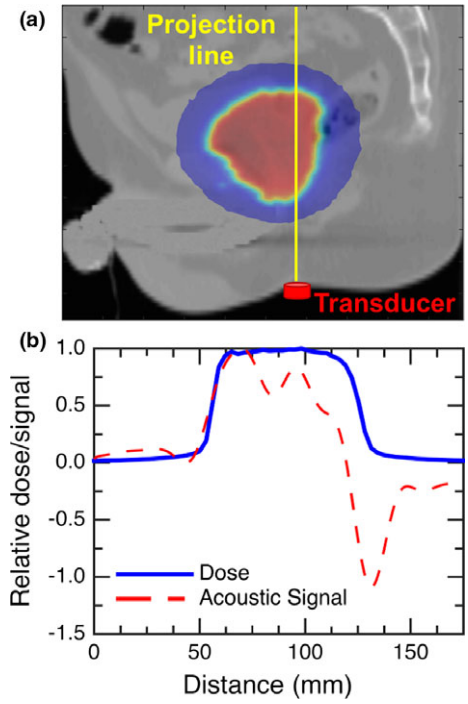

FIG. 4. (a) CT scan with the overlaid dose distribution for a lateral beam extracted from a VMAT delivery. The simulated transducer is placed at the perineum. (b) The transducer signal mapped into distance and compared to the dose profile along the detection line. Each boundary generates a bipolar pulse, and the transition between the two components of each pulse aligns with the dose gradient.

measurements of nonstandard radiation fields. Ideally, a commercial XACT system for water tank measurements would consist of a circular transducer array that encloses the radiation field. This would allow for the simultaneous acquisition of signals at different angles surrounding the field, and therefore rapid imaging.

XACT has numerous advantageous characteristics that make it a promising technique for water tank dosimetry applications. There is a linear relationship between deposited dose and induced pressure in a homogeneous medium. Additionally, XACT is dependent on the dose deposited per pulse, meaning it can be considered energy and dose rate independent.[37] Also, XACT does not perturb the radiation beam provided the transducers are placed outside the beam path. These features of XACT simplify calibration and eliminate the need for many of the correction factors required by other dosimetry techniques.

While previous work has been limited to 2D, XACT is inherently 3D due to the spherical propagation of acoustic waves, and 3D images could be reconstructed provided an appropriate transducer acquisition system is used. Initial studies have displayed relative XACT images; however, it could be possible to use XACT for absolute dosimetry measurements provided the heat defect, physical density and Grüneisen coefficient are accurately known, and the transducer and amplification system is well calibrated and characterized.

An important challenge of translating XACT into a viable clinical water tank dosimetry technique is the achievable resolution. Linac pulse envelope lengths typically range from 3 to 4 μs, which roughly translates into an in-water spatial resolution of 4.4 to 5.9 mm. It is possible to shorten the linac pulse length, but this is typically not done clinically and leads to decreased acoustic signal amplitude since less dose is deposited per pulse. Signal processing techniques such as deconvolution of the detected transducer signals from the linac pulse shape could be an interesting approach to resolve this problem provided the radiation pulse structure and signal acquisition system can be properly modelled.

Another key challenge of XACT is its sensitivity to detecting small amplitude acoustic waves. Lower energy beams are typically calibrated to deliver less dose per pulse than the higher energy flattening filter free beams used in previous XACT studies.[36] Improvements in detection amplification will be necessary to accurately image radiation fields delivered by 6 MV photon beams without the need for excessive signal averaging. Additionally, designing transducers or hydrophones with an appropriate central frequency and bandwidth for the intended application can further improve signal detection sensitivity.

More sophisticated signal processing and image reconstruction techniques are expected to be useful for obtaining higher quality XACT images. Previous studies used a simple back-projection algorithm for reconstruction. The resulting XACT images suffered from negative intensity ring artifacts, likely primarily caused by the finite bandwidth of the transducer. Applying iterative reconstruction algorithms,[40] particularly those with non-negative constraints,[41] could help solve this problem. The possibility of accounting for signal frequency components lost in detection should also be investigated to improve the accuracy of the reconstructed images.

The simulation studies described in Section 4.B indicate that XACT is a promising *in vivo* dosimetry technique as well. Since acoustic waves are induced and detected following a single pulse of radiation, XACT could provide a near real-time methodology for verifying treatment delivery as an alternative to using implanted and invasive dosimeters or relying on indirect exit dosimetry techniques.[42]

One of the most promising aspects of using XACT for *in vivo* dosimetry is the potential of combining it with anatomical ultrasound imaging. The use of intrafractional ultrasound imaging to monitor target motion during treatment is becoming increasingly more common,[43] and combining intrafractional ultrasound with XACT is an interesting possibility. Theoretically, the same transducer could be used to acquire B-mode anatomical ultrasound images and to detect radiation-induced acoustic signals, allowing the inherent registration of the ultrasound image with dosimetric information. One can imagine a system where the expected acoustic signal based on the patient plan is simulated prior to treatment, and treatment is halted if the acoustic signal detected during treatment deviates significantly from what is expected. Combined with ultrasound target tracking, this could allow for real-time

verification that dose is being delivered to the desired location in the patient. Additionally, the combination of XACT with anatomical ultrasound could allow for improved accuracy of dosimetric information, since knowledge regarding tissue heterogeneities could be extracted from the anatomical ultrasound image and considered during XACT image reconstruction.

Current commercial diagnostic ultrasound transducers will likely not be suitable for combined anatomical and dosimetry measurements due to the different frequency requirements of the two modalities. Anatomical imaging requires transducers with a central frequency between 3 and 10 MHz depending on the site, while the detection of induced acoustic waves is optimal with a wide bandwidth transducer with a central frequency in the hundreds of kHz frequency range. Thus, dual frequency transducers are likely to be required. Such transducers have been developed for ultrasound-guided high-intensity focused ultrasound (HIFU) applications, where a low frequency portion of the transducer is used for therapeutic purposes and the higher frequency region is used for imaging.[44] Similarly, dual frequency transducers have been developed for contrast enhanced harmonic ultrasound imaging.[45] While combined diagnostic ultrasound/XACT imaging will likely require the development of novel transducer technology, the principles behind the dual frequency transducers previously constructed for these other uses could be applicable.

Previous simulation studies have assessed the detection of acoustic signals both using an ultrasound array surrounding the patient[38] and using a single transducer.[39] While an array allows for 3D reconstruction of the dose distribution, the placement of transducers in such a geometry may be difficult due to radiation beam interference. However, it could be possible to account for transducers during the treatment planning stage,[46] and a recent study demonstrated the construction and operation of a radiolucent transducer.[47] Using a single transducer limits the amount of dosimetric information that can be extracted from detected acoustic signals, however, clinical implementation may become easier.

The integration of XACT into the clinical workflow will be aided by developments in intrafractional ultrasound imaging since many of the challenges arising from placing a transducer in contact with the patient during radiotherapy delivery have already been investigated in the literature. Intrafractional ultrasound imaging has been clinically demonstrated for tracking the target during prostate,[48] liver[49] and pancreas[50] treatments. Due to the same requirements for acoustic wave propagation for both XACT and diagnostic ultrasound, XACT is expected to be applicable to the same clinical sites that are accessible by diagnostic ultrasound, namely the breast, liver, kidney, pancreas, prostate, cervix, uterus, bladder, and rectum.[43]

Finally, it should be noted that while the previous discussion has focused on linac photon beam dosimetry, these concepts are also expected to be extendible to the dosimetry of electron beams produced by clinical linear accelerators.

5. PROTON THERAPY RANGE VERIFICATION

5.A. Motivation

A major, yet unsolved, issue in proton therapy is the ability to locate the maximum of energy deposition, i.e., the Bragg peak, ideally in real-time and noninvasively during patient treatment. Despite continued advances in the ability of computational models to accurately predict the therapeutic dose to be delivered,[51,52] several sources of uncertainties in the actual delivery remain. These uncertainties are mostly related to the calibration of x-ray CT imaging data into proton stopping power relative to water for treatment planning, in addition to set-up errors and possible anatomical variations during the course of fractionated therapy.[53] Currently, uncertainties in the proton beam range are on the order of 2.5–4.5%. In addition to this range-dependent uncertainty, 1–3 mm are added to range safety margins during treatment planning.[53] There is also careful consideration of beam angles to avoid the placement of the Bragg peak immediately before radiosensitive organs. Although such choices enable a safe delivery of treatment plans under consideration of the above mentioned range uncertainties, they restrict the possibilities of dose escalation due to the non-negligible exposure of healthy tissue, which generally limits full exploitation of the ballistic advantages offered by proton beams.

To this end, detection of secondary emissions for *in vivo* verification of the beam range is a very active area of research worldwide, aiming to reduce the above mentioned range uncertainties for safer delivery of more conformal treatments in the clinical practice. So far most of the studies already reaching clinical testing have been focused on bulky instrumentation aiming to detect primarily photon radiation resulting from nuclear-based interactions, so called positron emission tomography and prompt gamma imaging.[54,55]

On the other hand, interest was recently renewed in the exploitation of acoustic emissions, which are intrinsically related to the energy deposition process. In contrast to the already mentioned earlier attempts in the 1990s,[29] the trend of modern technologies with superposition of narrow pencil beams (so called pencil beam scanning,[56]), even intrinsically pulsed in the case of latest-generation compact proton therapy accelerators,[57] inherently favors generation of acoustic emissions according to Eqs. (11) and (12). Therefore, several groups are currently investigating proton-induced acoustic emissions (so called protoacoustics or, more generally, ionoacoustics) as a promising method to provide *in vivo* and real-time localization of selected pencil beams delivered to the patient, co-registered to tissue anatomy visualized with conventional ultrasound imaging for favorable sites of good sonic accessibility. Because of the already discussed relationship between energy deposition and acoustic emissions, this method might also open the longer-term perspective of reconstructing the actual dose delivery, at least for selected pencil beams generating sufficient acoustic signals, for novel concepts of adaptive therapy during a treatment course.

5.B. Recent work

There has been a recent resurgence of interest in thermoacoustic-based proton range verification. Due to the proliferation of proton therapy, expanded access to proton beams, and increased computational power, experimental and simulation work in the field has escalated following a decade-long lull since the 1990s experiments.[28,29]

To understand the potential of the technique, initial simulations focused on feasibility studies and exploring the information content of proton-induced acoustic waves. Alsanea et al. proposed radiation-induced acoustic computed tomography (RACT) in which the proton-induced acoustic signal measured by an array of transducers is used to reconstruct the 3D dose distribution through a filtered backprojection algorithm.[31,58] The reconstruction accuracy of clinical pencil beam dose depositions was investigated as a function of noise level and number of projection angles. For low noise levels (approximately equal to the maximum signal pressure amplitude), RACT showed sub-millimeter proton range verification and <2% dosimetric Bragg peak accuracy. Although promising, RACT requires multiple measurements — on the order of 10^3 detection points.

Previous[28,29] and subsequent studies have focused on range verification using one or a few transducers. Jones et al. simulated a pencil-beam proton dose deposition in a homogeneous water medium, and, consistent with previous experiments,[59] showed that it generates two macroscopic waves, labeled "α" and "γ".[60] The α-wave is generated by the cylindrical pre-Bragg peak portion of the dose deposition, and its arrival time is related to the distance between detector and beam axis. The γ-wave is induced by the Bragg peak, and its arrival time reports on the distance between the detector and the Bragg peak. For detectors placed at a depth greater than the Bragg peak, a single pressure wave (γ) is observed. Simulations confirmed previous intuition,[28,29] and later systematic studies by Albul et al.,[59] that through time-of-flight calculations the detector-to-Bragg-peak distance may be calculated by multiplying the γ-wave arrival time by the speed of sound in the medium.[60] Further simulation work showed that the central frequency of the proton-induced acoustic spectrum is <400 kHz, and predicted that the acoustic waves induced by a single proton pulse depositing on the order of 10^1–10^2 mGy are detectable by 5 cm diameter transducers even in the presence of thermal noise.[61]

As described in Eq. (15), thermoacoustic pressure waves depend on the temporal shape of the excitation pulse. If the pulse is shorter than the acoustic transit time across the Bragg peak's longitudinal dimension, stress confinement is achieved and the acoustic pressure waves are dictated by the spatial shape of the dose deposition. If the pulse is longer, stress confinement is not achieved and the acoustic waves are affected. Simulations examining the effect of proton pulse lengths concluded that the ideal proton pulse length and shape are on the cusp of stress confinement.[62] For clinical proton beams, Gaussian proton pulses with a full-width half-maximum (FWHM) of roughly 5 μs are expected to generate acoustic waves with the highest SNR per deposited dose assuming the acoustic signal is averaged over multiple proton pulse deliveries. The studies also found that SNR is maximized by increasing the instantaneous proton pulse intensity.

Recently, clinical experiments have been challenged by producing proton pulses with envelopes that are short enough to generate a detectable acoustic signal. Clinically common proton sources (cyclotron and synchrotron) deliver millisecond-to-second long macrostructure proton pulses.[63] Unlike joint clinical/research centers, which have the ability to dispense individual 50 ns synchrotron bunches separated by 50 ms periods,[28] clinical proton pulses consist of 0.5–50 ns microstructure bunches delivered at >5 MHz repetition rates.[55] Because this <200 ns repetition period is much smaller than the stress confinement criteria, the microstructure is undetectable in the acoustic signal and the pressure emissions are shaped by the macrostructure proton pulse envelope. The newest clinical sources, synchrocyclotrons, clinically deliver approximately 3.5 μs FWHM Gaussian proton pulses,[16] which are predicted to be ideal for acoustic wave generation.[62] To experimentally characterize proton-induced thermoacoustics, researchers have first used accessible non-clinical proton sources,[64,65] and modified others.[66] To generate detectable acoustic signals using a clinical IBA 230 cyclotron, Jones *et al.* modified the proton pulse output by modulating the proton current entering the cyclotron with a function generator.[66] With this method, they were able to generate approximately Gaussian proton pulses of roughly 17 μs FWHM, and the arrival times of the hydrophone-detected pressure waves were proportional to detector distance from the beam. Significant averaging was required due to noise. Other experiments using the same cyclotron modulation method (and the same 17 μs, non-ideal proton pulses) projected a precision in arrival time measurement of 2.2 mm (standard deviation) based on averaging signals induced by 2 Gy (at high currents of 10^8 protons per pulse) of deposited dose.[67] More recently, experiments in a water phantom were performed at the world's first clinical synchrocyclotron at the Centre Antoine-Lacassagne (CAL, Nice, France),[16] which delivered a pencil beam in proton pulses of about 3 μs pulse width and 1 kHz repetition rate, therefore ideal conditions for ionoacoustic range measurements not needing any further beam modifications. Using a hydrophone in axial geometry distal to the beam stopping point along with a trigger from a scintillator-based detector, the Bragg peak position could be measured with an accuracy and precision of better than 1 mm compared to Stringray ionization chamber based range measurements as well as Geant4 simulations, as seen in Fig. 5. However, 1000-fold averaging was necessary to obtain sufficient SNR, resulting in a Bragg peak dose of about 10 Gy. Nevertheless, all authors of the above mentioned studies identified future possibilities of signal enhancement when using multiple, and more sensitive detectors.

The proton-induced acoustic waves are bipolar. A positive compression peak reaches the detector first and is followed by a negative rarefaction peak. For non-RACT methods that seek to determine the proton range based on a time-of-flight

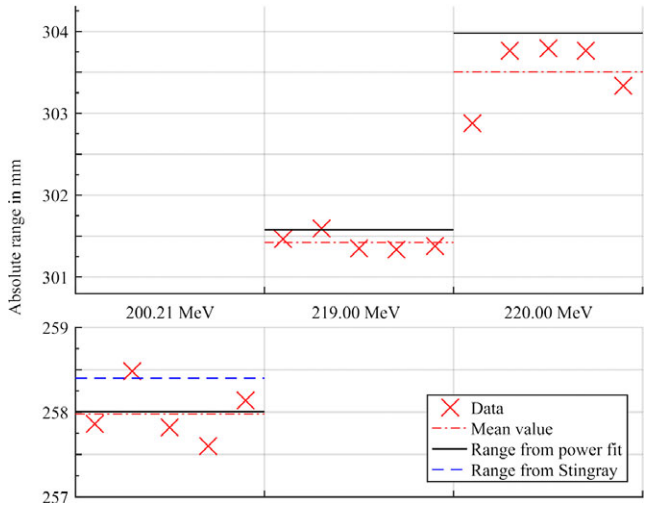

FIG. 5. Variation of repeated ionoacoustic range measurements at several energies, compared to a fit of existing Stingray data. For 200.21 MeV, Stingray range value was measured consecutively to the ionoacoustic data acquisition. Reproduced with permission from Ref. [16].

calculation (protoacoustics/ionoacoustics), the distance between detector and Bragg peak is calculated by multiplying the acoustic arrival time by the speed of sound in the medium. This raises the question of where to measure the arrival time. A number of methods have been used, including measuring the arrival time from the compression peak,[64] the midpoint between compression peak and rarefaction trough,[60] deconvolving the proton pulse,[67] and measuring from the earliest appearance of the pressure wave.[68] By projecting the cumulatively-integrated pressure waves measured at a few detectors, a beam-forming reconstruction has also been used.[69] Although the Bragg peak distance is close to that predicted by the zero cross-over point between compression and rarefaction peaks, there is no universally correct arrival time definition; the Bragg peak asymmetry imprints itself on the acoustic wave in a complicated way that depends on detector position.[62] Depending on the used arrival time definition, an offset might be required.[64] There is also ambiguity in the detector response that may introduce a delay that must be calibrated to accurately convert arrival time into distance.[16,67]

An additional intriguing feature of acoustic-based range verification is its possible combination with ultrasonic visualization of tissue anatomy, as discussed earlier with XACT for linac photon beam dosimetry. To this end, ionoacoustic measurements of the proton Bragg peak in combination with ultrasound and optoacoustic imaging was reported for the first time in an *ex vivo* mouse experiment at a nonclinical low-energy (approximately 20 MeV) pulsed proton source, as seen in Fig. 6.[70] In the same year, Patch et al. performed intrinsically co-registered ionoacoustic and ultrasonic acquisitions of water and a gelatine phantom by another specially manipulated non-clinical low-energy (50 MeV) proton source using a cardiac ultrasound transducer array.[65] This measurement required a signal integration of 1024 pulses corresponding to over 2000 Gy of total dose delivery. For clinical proton energies, dedicated devices will need to be developed in order to provide the required frequency spectra for ultrasound imaging (MHz) and proto/ionoacoustic sensing (kHz), ideally integrated in a single system for intrinsic co-registration. Such an advanced technology could enable near real-time visualization of the Bragg peak position superimposed on the tissue anatomy for verification of the beam delivery on a spot-by-spot basis, ideally enabling image guided compensation of tumor motion.

All of the recent work described above, with the notable exception of Ref. [70], has been performed in homogeneous materials, almost exclusively water. Translating the acoustic-based proton range verification technique from water to heterogeneous tissue presents a number of challenges. The tissue heterogeneity manifests itself in two ways: (a) the initial pressure distribution will vary with the Grüneisen coefficient [Eq. (8)] of the underlying tissue, and (b) the acoustic wave propagation will be affected by the tissue-dependent speed of sound, attenuation, and reflection. Of these, the speed of sound dependence appears to be the most challenging hurdle for accurate range verification because the time-of-flight calculation requires knowledge of the speed of sound. To understand the effects of heterogeneity, CT-based k-Wave simulations have been performed that assign the Grüneisen coefficient and speed of sound to each voxel based on the tissue type, as determined by Hounsfield Unit value.[69,71] Simulations by Patch et al. predict that accurate range verification is achievable during a clinical prostate treatment using a transrectal probe. By comparing the measured acoustic wave arrival times to a precalculated simulated dataset, local heterogeneity-induced variations could be corrected to give <2 mm errors in range calculation accuracy.[69] Another set of simulations compared the acoustic propagation of the same initial pressure distribution over homogeneous water and heterogeneous liver and prostate sites, as shown in Fig. 7.[71] For the considered liver case, tissue attenuation was only about 1 dB, and the average speed of sound between detectors and the Bragg peak differed by ≤2.2% compared to the speed of sound in water. For the few considered prostate beams, short proton pulses may allow for proton range verification with an accuracy of <2 mm if the detectors are placed distal to the Bragg peak and the beam propagation axis is known a priori.[71]

5.C. Future outlook

The promising results reported by several groups encourage the ongoing efforts to overcome one of the major remaining challenges of ionoacoustic range verification, namely improving the SNR for monitoring individual pencil beams at typical therapeutic doses. Along with possibilities of signal enhancement at the clinical proton sources with proper beam pulsing and elevated instantaneous dose rate, detector technologies can also be advanced to enable utmost sensitivity in the relatively low frequency range (10–100 kHz) of proton-induced acoustic emissions, ideally in combination with ultrasound imaging. Moreover, utilization of multiple

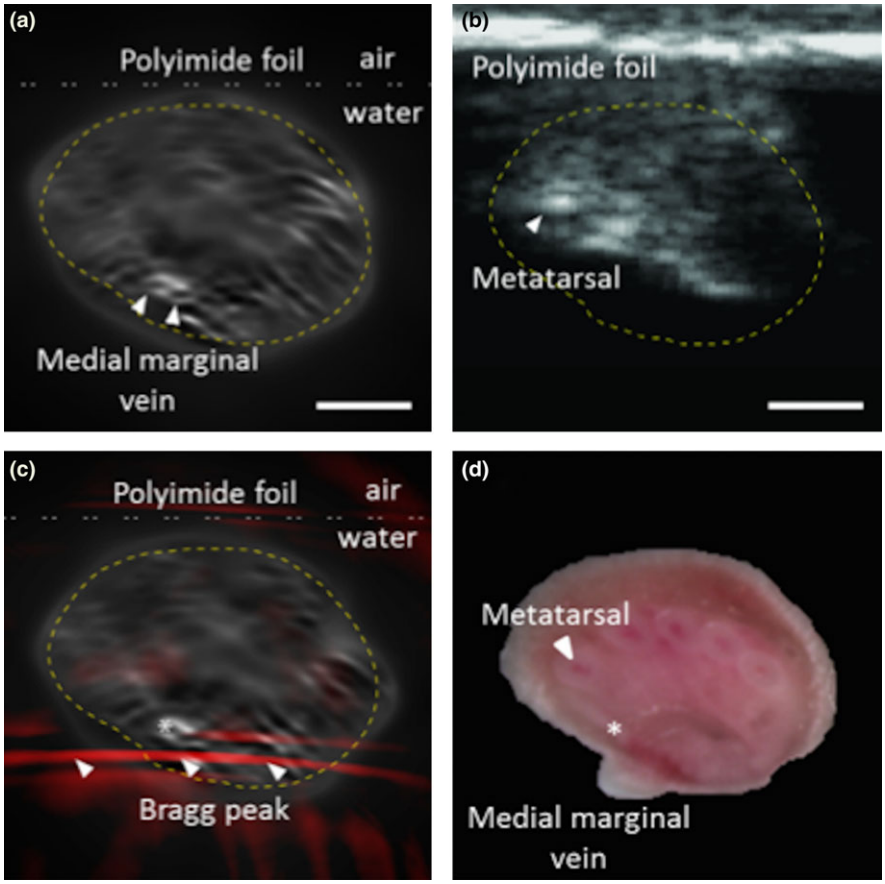

FIG. 6. First time triple-modality imaging of a mouse leg using (a) optoacoustics, (b) ultrasonography, (c) ionoacoustics in red marking the Bragg peak location and co-registered to the optoacoustics image. (d) A cryoslice of the mouse leg, where the star indicates the medial marginal vein. The scale in figures (a) and (b) represents 2 mm. Reprinted with permission from Ref. [70].

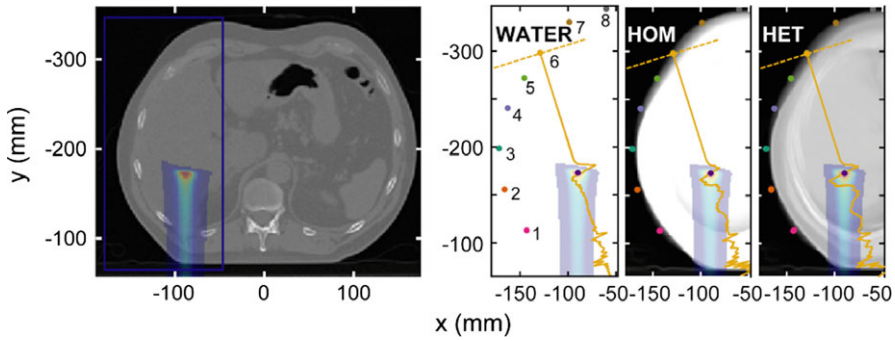

FIG. 7. The acoustic waves induced by a single proton pencil beam were simulated in a 3D CT liver volume (a transverse slice is shown at left). To characterize the effects of heterogeneity, the acoustic waves were propagated in water, a homogeneous tissue volume, and a heterogeneous tissue volume. Pressure traces simulated at detector position 6 are overlaid onto the images. Reproduced with permission from Ref. [71].

detectors — as already envisioned in the seminal Hayakawa et al. paper[29] — can offer an elegant means to overcome the issue of local heterogeneities. Although no multielement, low frequency arrays have yet been used in the context of acoustic-based proton range verification, triangulation with as few as 3–5 detectors[69,72] is expected to improve SNR and minimize errors introduced by heterogeneous tissue.[71]

Future conceivable clinical workflows could enable verification of the entire delivery for intrinsically pulsed clinical synchrocyclotrons, or pretreatment range verification of a few "diagnostic spots"[64,66] from artificially pulsed beams of conventional synchrotrons or cyclotrons. Along with the already discussed integration of ultrasound imaging, proto/ionoacoustic sensing could thus offer a unique, compact and cost-effective means for real-time range verification, and ideally even dose reconstruction of modern proton treatments, with co-registered anatomical confirmation. This could be especially beneficial for those critical tumor indications which are

currently challenged by intrafractional organ motion, such as prostate, breast, liver, and pancreas,[64] thus promising an important step forward in treatment quality and likely long-term outcomes.

6. MEDICAL IMAGING

6.A. Motivation

Since Wilhelm Conrad Roentgen discovered the x ray more than one hundred years ago, x-ray imaging has been an invaluable tool in medical diagnosis, biology, and materials science.[73–82] In particular, x-ray computed tomography (CT) has proven tremendously useful for non-invasive medical imaging since its inception nearly 50 yr ago.[83] However, CT requires a large set of projection data and high radiation dose to achieve sufficient image quality. It is estimated that up to 2% of cancer cases are the result of the radiation obtained from CT imaging,[84,85] thus this risk potentially negates many of the benefits. XACT takes advantage of high sensitivity to x-ray absorption and high ultrasonic resolution in a single modality.[86] A single projection x-ray exposure is sufficient to generate acoustic signals in 3D space since the x ray generated acoustic waves are of a spherical nature and propagate in all directions from their point of generation. While CT relies upon a rotating x-ray source and many x-ray projections to obtain a 3D image, XACT can generate a 3D image through a single x-ray projection, drastically decreasing radiation dose.

It should be noted that unlike the XACT applications described in Section 4, which use the acoustic emissions induced by therapeutic megavoltage x-ray beams to reconstruct the deposited dose, in the medical imaging application described here a diagnostic x-ray exposure is used to image the underlying structure based on contrast originating predominantly from differential photoelectric effect cross sections and underlying Grüneisen coefficients.

6.B. Recent work

XACT imaging as a novel biomedical imaging modality was first proposed and demonstrated in 2013,[30] and has since been studied by different groups all over the world in various applications.[33,35,36,38] Initially, systems with a single low central frequency ultrasound transducer were used for x-ray-induced acoustic signal collection in XACT imaging studies. A typical XACT imaging system with a single ultrasound transducer requires mechanical scanning for acquisition of a two-dimensional (2D) image, requiring multiple x-ray pulses and leading to long scan times.[30,36,86]

Recently, a new XACT imaging system that yields rapid and high resolution two dimensional images was developed and tested. A schematic of this system is shown in Fig. 8.[87] In this system, a sample is irradiated by a nanosecond-pulsed x-ray source, leading to the isotropic emission of acoustic waves. Instead of using a single transducer for detection, a ring array of piezoelectric ultrasound transducers detects the acoustic waves and converts them to electrical signals. The resulting signals are then back-projected to reconstruct the image. It should be noted that as this current system is using a ring-array of transducers, only a single 2D slice of the sample can be obtained. 3D imaging would be possible with a spherical or cup-shaped array.

Fig. 9 highlights key results from recent XACT studies. Figure 9(a) displays the XACT image of 150 μm thick

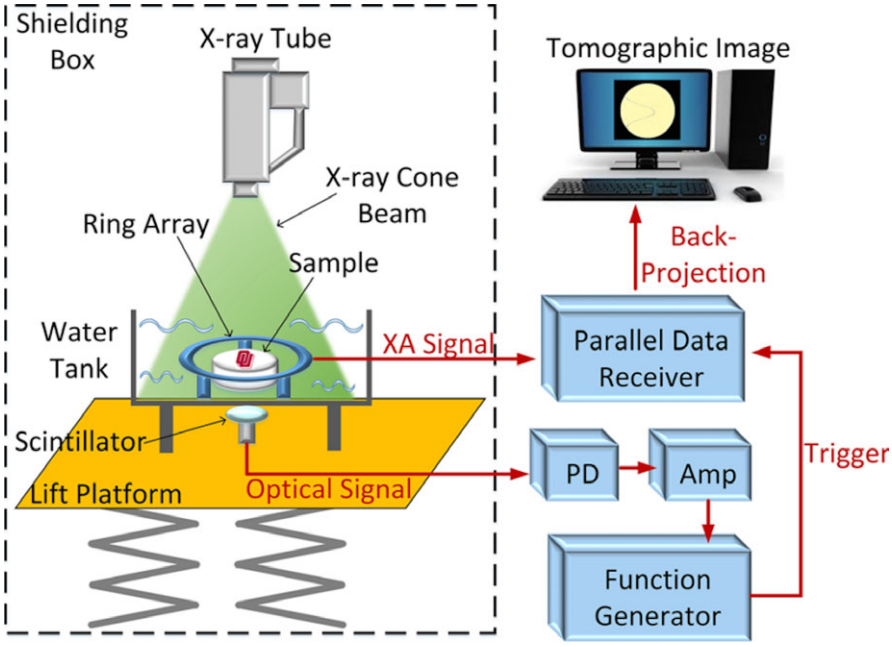

FIG. 8. Schematic diagram of XACT imaging system. A scintillator/photodiode combination is activated by the X-rays and is used to trigger the data receiver to start collecting signals from the ultrasound transducer array. Reprinted with permission from Ref. [87].

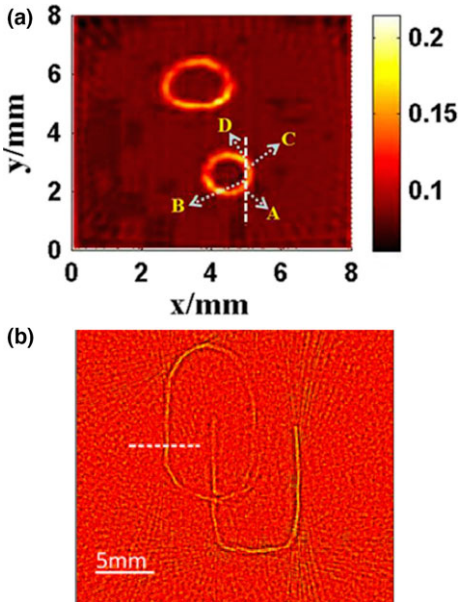

FIG. 9. (a) X-ray acoustic computed tomography image of gold fiducial markers. Reprinted with permission from Ref. [86]. (b) Lead OU logo XACT image. Reprinted with permission from Ref. [87].

gold fiducial markers acquired using a 60 ns x-ray source and single 2.25 MHz transducer. The image was shown to be in good agreement with the corresponding CT image, and based on the size of the reconstructed gold fiducial markers XACT spatial resolution was determined to be 350 μm.[86] Figure 9(b) shows an XACT image of lead sheets with thickness 150 μm shaped into the OU logo obtained using the fast XACT imaging system with the 5 MHz transducer array. This experiment resulted in a spatial resolution of 138 μm.[87]

6.C. Future outlook

Challenges encountered during these experiments were primarily due to equipment limitations. The images in Fig. 9 required a large number of x-ray pulses to obtain sufficient SNR. This large number of pulses can be reduced by two methods, both of which, at the time of writing, are being investigated. The first is to increase the amplification of each transducer in the ring array, as they are currently amplified at only 52 dB. An amplifier with enough channels to match each transducer element on the ring-array is necessary to do this. Second, the fluence of the x-ray tube can be increased with new x-ray sources, such as the laser-driven Thomson x-ray source.[88,89]

It is believed that XACT imaging will find broad applications in both basic research and clinical care. Considering the use of XACT in breast imaging, minimal x-ray exposure can generate a 3D acoustic image of the breast,[90] which dramatically reduces the radiation dose to patients when compared to conventional breast CT. Bone mineral density mapping could also be another possible application for XACT.

7. CONCLUSIONS

Based on the promising studies summarized in this article, ionizing radiation-induced acoustics based technologies have the potential to be highly useful, real-time, and cost-effective tools in three distinct applications. First, XACT could be a powerful tool for both relative and *in vivo* linac photon beam dosimetry, with the potential for development of a system combining XACT and anatomical ultrasound to visualize the delivered dose distribution in near real-time. Second, protoacoustics/ionoacoustics is a promising tool to accurately localize the Bragg peak and provide range verification for particle therapy, again with the potential to be combined with anatomical ultrasound to overlay the position of the Bragg peak on patient anatomy during treatment. Finally, XACT has the potential to be an effective low-dose diagnostic imaging modality for sites such as breast cancer.

Various technological advances are still required to bring these technologies to the clinic. Studies in all three areas reported a need for the development of novel transducer technologies. In the case of linac photon beam dosimetry and proton therapy range verification applications, novel low frequency transducers with a wide bandwidth are required. Ideally, dual frequency transducers need to be developed to enable the combination of induced acoustic wave detection and anatomical ultrasound imaging. Noise is a current limitation in all three areas, thus the development of highly sensitive transducers in the appropriate frequency range will be required for accurate signal detection at clinically relevant dose levels. Additionally, optimization of beam delivery technology will aid in the development of ionizing radiation-induced acoustics techniques. This may take the form of exploiting emerging radiation delivery devices, such as laser driven x-ray sources for medical imaging and synchrocyclotrons for Bragg peak localization, or adapting current radiation delivery technologies, such as decreasing the pulse length of therapeutic linacs or introducing a pulsed beam structure into clinical cyclotrons and synchrotrons used for proton beam therapy.

With the appropriate technological advances and further work investigating how these promising initial studies can be translated into the clinical setting, ionizing radiation-induced acoustics-based techniques are expected to have a significant clinical impact to guide cancer treatment delivery and imaging in the near future.

ACKNOWLEDGMENTS

S. H. acknowledges support by the NSERC CREATE Medical Physics Research Training Network grant 432290.

CONFLICT OF INTEREST

The authors have no conflicts to disclose.

[a]Author to whom correspondence should be addressed. Electronic mail: susannah.hickling@mail.mcgill.ca

REFERENCES

1. Bell AG. On the production and reproduction of sound by light. *Am J Sci*. 1880;20:305–324.
2. Bowen T. Radiation-induced thermoacoustic soft tissue imaging. In: *IEEE Ultrasonics Symposium Proceedings*; 1981:817–822.
3. Wang L, Hu S. Photoacoustic tomography: in vivo imaging from organelles to organs. *Science*. 2012;335:1458–1462.
4. Zackrisson S, van de Ven SMWY, Gambhir SS. Light in and sound out: emerging translational strategies for photoacoustic imaging. *Cancer Res*. 2014;74:979–1004.
5. Gao F, Feng X, Zheng Y. Advanced photoacoustic and thermoacoustic sensing and imaging beyond pulsed absorption contrast. *J Opt*. 2016;18:074006.
6. Kron T, Lehmann J, Greer PB. Dosimetry of ionising radiation in modern radiation oncology. *Phys Med Biol*. 2016;61:R167–R205.
7. Kawrakow I. Accurate condensed history Monte Carlo simulation of electron transport. I. EGSnrc, the new EGS4 version. *Med Phys*. 2000;27:485–498.
8. Agostinelli S, Allison J, Amako K, et al. GEANT4 – a simulation toolkit. *Nucl Instrum Methods Phys Res A*. 2003;506:250–303.
9. Forster R, and Godfrey T. MCNP – a general Monte Carlo code for neutron and photon transport. *Monte Carlo Methods Appl*. 1985;240:33–55.
10. Ferrari A, Sala PR, Fasso A, Ranft J. FLUKA: a multi-particle transport code. Tech. Rep. CERN-2005-10, Geneva; 2005.
11. Baro J, Sempau J, Fernandez-Varea J, Salvat F. PENELOPE: an algorithm for Monte Carlo simulation of the penetration and energy loss of electrons and positrons in matter. *Nucl Instrum Methods Phys Res B*. 1995;100:31–46.
12. Ross CK, Klassen NV, Shortt K, Smith G. A direct comparison of water calorimetry and Fricke dosimetry. *Phys Med Biol*. 1989;34:23–42.
13. Cox BT, Laufer JG, Beard PC. The challenges for quantitative photoacoustic imaging. *Proc SPIE*. 2009;7177:717713–717713–9.
14. Zhou Y, Yao J, Wang LV. Tutorial on photoacoustic tomography. *J Biomed Opt*. 2016;21:061007.
15. Hickling S, Leger P, El Naqa I.. On the detectability of acoustic waves induced following irradiation by a radiotherapy linear accelerator. *IEEE Trans Ultrason Ferroelectr Freq Control*. 2016;63:683–690.
16. Lehrack S, Assmann W, Bertrand D, et al. Submillimeter ionoacoustic range determination for protons in water at a clinical synchrocyclotron. *Phys Med Biol*. 2017;62:19–30.
17. Kruger R, Liu P, Fang Y, Appledorn C. Photoacoustic ultrasound (PAUS)- Reconstruction tomography. *Med Phys*. 1995;22:1605–1609.
18. Xu M, Wang L. Universal back-projection algorithm for photoacoustic computed tomography. *Phys Rev E*. 2005;71:016706.
19. Huang D-H, Liao C-K, Wei C-W, Li P-C. Simulations of optoacoustic wave propagation in light-absorbing media using a finite-difference time-domain method. *J Acoust Soc Am*. 2005;117:2795–2801.
20. Mast TD, Souriau LP, Liu DL, Tabei M, Nachman AI, Waag RC. A k-space method for large-scale models of wave propagation in tissue. *IEEE Trans Ultrason Ferroelectr Freq Control*. 2001;48:341–354.
21. Treeby BE, Cox BT. k-Wave: MATLAB toolbox for the simulation and reconstruction of photoacoustic wave fields. *J Biomed Opt*. 2010;15:021314.
22. Treeby BE, Cox BT. Modeling power law absorption and dispersion for acoustic propagation using the fractional Laplacian. *J Acoust Soc Am*. 2010;127:2741–2748.
23. Sulak L, Armstrong T, Baranger H, et al. Experimental studies of the acoustic signature of proton beams traversing fluid media. *Nucl Instrum Methods*. 1979;161:203–217.
24. Sachse W, Kim KY. Observation of x-ray generated ultrasound. In: *IEEE Ultrasonics Symposium Proceedings*; 1983: 677–680.
25. Mascarenhas S, Vargas H, Cesar CL. A photoacoustical radiation dosimeter. *Med Phys*. 1984;11:73–74.
26. Bowen T, Connor WG, Nasoni RL, et al. Observation of acoustic signals from a phantom in an 18 MeV electron beam for cancer therapy. In: *Acoustical Imaging*. New York: Plenum Press; 1984:429–434.
27. Bowen T, Chen CX, Liew SC, Lutz WR, Nasoni RL. Observation of ultrasonic emission from edges of therapeutic x-ray beams. *Phys Med Biol*. 1991;36:537–539.
28. Tada J, Hayakawa Y, Hosono K, Inada T. Time resolved properties of acoustic pulses generated in water and in soft tissue by pulsed proton beam irradiation – a possibility of doses distribution monitoring in proton radiation therapy. *Med Phys*. 1991;18:1100–1104.
29. Hayakawa Y, Tada J, Arai N, et al. Acoustic pulse generated in a patient during treatment by pulsed proton radiation beam. *Radiat Oncol Invest*. 1995;3:42–45.
30. Xiang L, Han B, Carpenter C, Pratx G, Kuang Y, Xing L. X-ray acoustic computed tomography with pulsed x-ray beam from a medical linear accelerator. *Med Phys*. 2013;40:010701.
31. Stantz K, Alsanea F, Moskvin V. Use of radiation-induced ultrasound to image proton dosimetry. *Med Phys*. 2013;40:546.
32. International Atomic Energy Agency. Development of procedures for in vivo dosimetry in radiotherapy. *IAEA Human Health Reports*. Vol. 8; 2013.
33. Kim J, Park E-Y, Jung Y, et al. X-ray acoustic-based dosimetry using a focused ultrasound transducer and a medical linear accelerator. *IEEE Trans Radiat Plasma Med Sci*. 2017;1:534–540.
34. Diao X, Zhu J, Li W, et al. Broadband detection of dynamic acoustic emission process induced by 6 MV therapeutic x-ray beam from a clinical linear accelerator. In: *IEEE International Ultrasonics Symposium Proceedings*; 2015:1–4.
35. Sampaio DRT, Uliana JH, Antonio AO, Pavoni JF, Pavan TZ. X-ray acoustic imaging for external beam radiation therapy dosimetry using a commercial ultrasound scanner. In: *IEEE International Ultrasonics Symposium Proceedings*; 2015:1–4.
36. Hickling S, Lei H, Hobson M, Leger P, Wang X, El Naqa I. Experimental evaluation of x-ray acoustic computed tomography for radiotherapy dosimetry applications. *Med Phys*. 2017;44:608–617.
37. Hickling S, Hobson M, El Naqa I. Characterization of x-ray acoustic computed tomography for applications in radiotherapy dosimetry. *IEEE Trans Radiat Plasma Med Sci*. 2018;1.
38. Hickling S, Hobson M, El Naqa I. Feasibility of x-ray acoustic computed tomography as a tool for noninvasive volumetric in vivo dosimetry. *Int J Radiat Oncol Biol Phys*. 2014;90:S843.
39. Hickling S, Hobson M, Renaud M, El Naqa I. In vivo detection of radiation-induced acoustic waves for treatment delivery verification: a simulation study. *Med Phys*. 2017;44:2760.
40. Paltauf G, Viator JA, Prahl SA, Jacques SL. Iterative reconstruction algorithm for optoacoustic imaging. *J Acoust Soc Am*. 2002;112:1536–1544.
41. Ding L, Deán-Ben XL, Lutzweiler C, Razansky D, Ntziachristos V. Image reconstruction in cross-sectional optoacoustic tomography based on non-negative constrained model-based inversion. In: *Proc SPIE*. 2015;9539:953919–953924.
42. Mijnheer B, Beddar S, Izewska J, Reft C. In vivo dosimetry in external beam radiotherapy. *Med Phys*. 2013;40:070903.
43. O'Shea T, Bamber J, Fontanarosa D, van der Meer S, Verhaegen F, Harris E. Review of ultrasound image guidance in external beam radiotherapy part II: intra-fraction motion management and novel applications. *Phys Med Biol*. 2016;61:R90–R137.
44. Azuma T, Ogihara M, Kubota J, Sasaki A, Umemura SI, Furuhata H. Dual frequency ultrasound imaging and therapeutic bilaminar array using frequency selective isolation layer. *IEEE Trans Ultrason Ferroelectr Freq Control*. 2010;57:1211–1224.
45. Martin K, Lindsey B, Ma J, et al. Dual frequency piezoelectric transducers for contrast enhanced ultrasound imaging. *Sensors*. 2014;14:20825–20842.
46. Bazalova-Carter M, Schlosser J, Chen J, Hristov D. Monte Carlo modeling of ultrasound probes for image guided radiotherapy. *Med Phys*. 2015;42:5745–5756.
47. Schlosser J, Hristov D. Radiolucent 4D ultrasound imaging: system design and application to radiotherapy guidance. *IEEE Trans Med Imaging*. 2016;35:2292–2300.
48. Trivedi A, Ashikaga T, Hard D, et al. Development of 3-dimensional transperineal ultrasound for image guided radiation therapy of the prostate: early evaluations of feasibility and use for inter- and intrafractional prostate localization. *Pract Radiat Oncol*. 2016;7:e27–e33.

49. Schlosser J, Gong RH, Bruder R, et al. Robotic intrafractional US guidance for liver SABR: system design, beam avoidance, and clinical imaging. *Med Phys*. 2016;43:5951–5963.
50. Omari EA, Erickson B, Ehlers C, et al. Preliminary results on the feasibility of using ultrasound to monitor intrafractional motion during radiation therapy for pancreatic cancer. *Med Phys*. 2016;43:5252–5260.
51. Bauer J, Sommerer F, Mairani A, et al. Integration and evaluation of automated Monte Carlo simulations in the clinical practice of scanned proton and carbon ion beam therapy. *Phys Med Biol*. 2014;59:4635–4659.
52. Verburg JM, Grassberger C, Dowdell S, Schuemann J, Seco J, Paganetti H. Automated Monte Carlo simulation of proton therapy treatment plans. *Technol Cancer Res Treat*. 2016;15:NP35–NP46.
53. Paganetti H. Range uncertainties in proton therapy and the role of Monte Carlo simulations. *Phys Med Biol*. 2012;57:99–117.
54. Parodi K. Vision 20/20: positron emission tomography in radiation therapy planning, delivery, and monitoring. *Med Phys*. 2015;42:7153–7168.
55. Krimmer J, Dauvergne D, Létang JM, Testa É. Prompt-gamma monitoring in hadrontherapy: a review. *Nucl Instrum Methods Phys Res A*. 2018;878:58–73.
56. Pedroni E, Bacher R, Blattmann H, et al. The 200-MeV proton therapy project at the Paul Scherrer Institute: conceptual design and practical realization. *Med Phys*. 1995;22:37–53.
57. Henrotin S, Abs M, Forton E, et al. Commissioning and testing of the first Iba S2C2. In: *Proceedings of Cyclotrons 2016*; 2016:178–180.
58. Alsanea F, Moskvin V, Stantz KM. Feasibility of RACT for 3D dose measurement and range verification in a water phantom. *Med Phys*. 2015;42:937–946.
59. Albul VI, Bychkov VB, Vasil'ev S, et al. Acoustic field generated by a beam of protons stopping in a water medium. *Acoust Phys*. 2005;51:33–37.
60. Jones KC, Witztum A, Sehgal CM, Avery S. Proton beam characterization by proton-induced acoustic emission: simulation studies. *Phys Med Biol*. 2014;59:6549–6563.
61. Ahmad M, Xiang L, Yousefi S. Xing L. Detection threshold of proton-acoustic range verification. *Med Phys*. 2015;42:5735–5744.
62. Jones KC, Seghal CM, Avery S. How proton pulse characteristics influence protoacoustic determination of proton-beam range: simulation studies. *Phys Med Biol*. 2016;61:2213–2242.
63. International Commission on Radiation Units and Measurements. Prescribing, recording, and reporting proton-beam therapy (ICRU Report 78). tech. rep., ICRU, Bethesda; 2007.
64. Assmann W, Kellnberger S, Reinhardt S. et al. Ionoacoustic characterization of the proton Bragg peak with submillimeter accuracy. *Med Phys*. 2015;42:567–574.
65. Patch SK, Kireeff Covo M, Jackson A. et al. Thermoacoustic range verification using a clinical ultrasound array provides perfectly co-registered overlay of the Bragg peak onto an ultrasound image. *Phys Med Biol*. 2016;61:5621–5638.
66. Jones KC, Stappen FV, Bawiec CR, et al. Experimental observation of acoustic emissions generated by a pulsed proton beam from a hospital-based clinical cyclotron. *Med Phys*. 2015;42:7090–7097.
67. Jones KC, Vander Stappen F, Sehgal CM, Avery S. Acoustic time-of-flight for proton range verification in water. *Med Phys*. 2016;43:5213–5224.
68. Nie W, Jones KC, Petro S, Kassaee A, Sehgal CM, Avery S. Proton range verification in homogeneous materials through acoustic measurements. *Phys Med Biol*. 2018;63:025036.
69. Patch SK, Hoff DEM, Webb TB, Sobotka LG, Zhao T. Two-stage ionoacoustic range verification leveraging Monte Carlo and acoustic simulations to stably account for tissue inhomogeneity and accelerator-specific time structure – a simulation study. *Med Phys*. 2017;45:783–793.
70. Kellnberger S, Assmann W, Lehrack S, et al. Ionoacoustic tomography of the proton Bragg peak in combination with ultrasound and optoacoustic imaging. *Sci Rep*. 2016;6:29305.
71. Jones K, Nie W, Chu J, et al. Acoustic-based proton range verification in heterogeneous tissue: simulation studies. *Phys Med Biol*. 2018;63:025018.
72. Kundu T. Acoustic source localization. *Ultrasonics*. 2014;54:25–38.
73. Dierolf M, Menzel A, Thibault P, et al. Ptychographic X-ray computed tomography at the nanoscale. *Nature*. 2010;467:436–439.
74. Gaffney KJ, Chapman HN. Imaging atomic structure and dynamics with ultrafast X-ray scattering. *Science*. 2007;316:1444–1448.
75. Miao J, Ishikawa T, Robinson IK, Murnane MM. Beyond crystallography: diffractive imaging using coherent x-ray light sources. *Science*. 2015;348:530–535.
76. Neutze R, Wouts R, van der Spoel D, Weckert E, Hajdu J. Potential for biomolecular imaging with femtosecond X-ray pulses. *Nature*. 2000;406:752–757.
77. Robinson AL. High-resolution imaging with soft x-rays. *Science*. 1982;215:150–152.
78. Robinson AL. Imaging unaltered cell structures with x-rays. *Science*. 1987;237:723–724.
79. Rowlands JA. Material change for X-ray detectors. *Nature*. 2017;550:47.
80. Schroer CG. X-ray imaging: the chemistry inside. *Nature*. 2011;476:159.
81. Service RF. Brilliant X-rays reveal fruits of a brilliant mind. *Science*. 2006;313:744.
82. Tegze M, Faigel G, Marchesini S, Belakhovsky M, Ulrich O. Imaging light atoms by X-ray holography. *Nature*. 2000;407:38.
83. Robinson AL. Image reconstruction (I): computerized X-ray scanners. *Science*. 1975;190:542–593.
84. Lin EC. Radiation risk from medical imaging. *Mayo Clin Proc*. 2010;85:1142–1146.
85. Hobbs JB, Goldstein N, Lind KE, Elder D, Dodd GD, Borgstede JP. Physician knowledge of radiation exposure and risk in medical imaging. *J Am Coll Radiol*. 2018;15:34–43.
86. Xiang L, Tang S, Ahmad M, Xing L. High resolution x-ray-induced acoustic tomography. *Sci Rep*. 2016;6:26118.
87. Tang S, Nguyen DH, Zarafshani A, et al. X-ray-induced acoustic computed tomography with an ultrasound transducer ring-array. *Appl Phys Lett*. 2017;110:103504.
88. Umstadter DP. All-laser-driven Thomson X-ray sources. *Contemp Phys*. 2015;56:417–431.
89. Chen S, Golovin G, Miller C, et al. Shielded radiography with a laser-driven MeV-energy X-ray source. *Nucl Instrum Methods Phys Res Sect B*. 2016;366:217–223.
90. Tang S, Yang K, Chen Y, Xiang L. X-ray-induced acoustic computed tomography for 3D breast imaging: a simulation study. *Med Phys*. 2018;45:1662–1672.